2020

Determination of Zirconium Oxide Chemistry Through Complementary Characterization Techniques

Corey M. Efaw
Boise State University

Reynolds Michael
Boise State University

Jordan L. Vandegrift
Boise State University

Kassiopeia Smith
Boise State University

Yaqiao Wu
Boise State University

See next page for additional authors

DETERMINATION OF ZIRCONIUM OXIDE CHEMISTRY THROUGH COMPLEMENTARY CHARACTERIZATION TECHNIQUES

Corey M. Efaw,[1] Michael Reynolds,[1] Jordan L. Vandegrift,[1,2] Kassiopeia Smith,[1,2] Yaqiao Wu,[1,2] Brian J. Jaques,[1,2] Hongqiang Hu,[3] Claire Xiong,[1] Michael F. Hurley[1]

1. *Boise State University, 1910 W University Dr, Boise, ID, 83725*
2. *Center for Advanced Energy Studies, 995 University Blvd, Idaho Falls, ID 83401*
3. *Idaho National Laboratory, 2525 Fremont Ave, Idaho Falls, ID 83402*

Nuclear energy has been increasingly recognized as an effective and low carbon-emission energy source. Nuclear reactors are susceptible to adverse effects, which can lead to potentially severe consequences, though they are low in probability. To ensure safety and improved monitoring of reactors, there have been increasing interests in developing sensors to monitor key parameters relating to the status within a reactor. In order to improve sensor accuracy, high-resolution characterization of cladding materials can be utilized to correlate with sensor output. A common issue with zirconium cladding is the so-called "breakaway phenomenon", a critical factor seen as the transition from an initially passive zirconia to an active material. Existing research presents many factors that contribute to the breakaway mechanism, ultimately resulting in difficulty to predict its activation and propagation. As part of the effort to develop sensors, an improved understanding of pre- and post-breakaway zirconium alloys (Zr, Zr-2.65Nb, Zry-3, and Zry-4) is accomplished with Raman spectroscopy, scanning Kelvin probe force microscopy, and atom probe tomography.

I. INTRODUCTION

Within a nuclear core, uranium-based fuels release multiple high energy neutrons by fission and cause a chain reaction, generating useable energy for our society's ever-increasing power demands. To allow a fission chain reaction to occur unperturbed and generate energy efficiently, a cladding material encapsulates the fuel, preventing highly radioactive fission products from escaping into the surrounding coolant. Zirconium is a viable material choice for cladding due to its low neutron absorption cross-section, high mechanical strength, and strong corrosion resistance while in an extreme environment.[1] Alloying of zirconium has been shown to increase cladding performance by improving mechanical properties and corrosion resistance in high-temperature water.[2-6]

The general high-temperature coolant-side corrosion of zirconium cladding is similar regardless of oxidizing media (oxygen, water, or steam).[7] Initial formation of the oxide film provides a passivating film, thus slowing the rate of oxidation to follow empirical power-law with parabolic to sub-parabolic characteristics (exponent, $n \leq 0.5$). Here, the kinetics are limited by diffusion of corrosion species to the metal/oxide interface.[8] With subsequent oxidation, cracks develop within the oxide, providing pathways for species to reach the base metal at an increased rate. This is observed as a transition in mass growth, progressing to an increased oxidation rate.[8-11] This is commonly termed as the "breakaway phenomenon".[9] Depending on alloy composition, some elements support cyclic transition between passivation and oxidation, while others do not support re-passivation and the alloy fails to recover from the first breakaway. Regardless, continuous oxidation of the metal eventually leads to failure of the cladding material, albeit at different rates.[9, 10]

In addition to the breakaway phenomenon, there are other effects that contribute to cladding failure. Addition of hydrogen species in the coolant has been shown to cause cladding embrittlement by dendrite-like precipitation in the metal.[2, 12, 13] Inclusion of nitrogen species has been found to advance the breakaway phenomenon by creating defects and lattice mismatch in the oxide, thus permitting increased oxygen diffusion to the base metal.[14-21] Additional effects such as high compressive stresses,[10, 22-27] zirconia phase content,[16, 17, 20, 28-30] sub-stoichiometry of the oxide,[7, 15-17] operating temperature,[31-34] and alloying dopants[2, 8, 12, 24, 25, 35] are all believed to play a role in cladding failure. Additional contributions from the fuel/cladding interface, such as fuel swelling,[36] fuel fracture,[37] and stress corrosion cracking lead to unpredictable cladding lifetime, as well as decreased energy efficiency. The complexity of differing effects presents a difficult problem to predict cladding failure, and thus has been a major focus of nuclear research.

Presently, chemical evolution over the lifetime of the fuel and cladding inside a nuclear reactor can only be inferred using post-irradiation examination (PIE).[38] Due to

the adverse environment created from harsh ambient conditions and irradiation, the corrosion mechanisms of cladding are difficult to observe in-core or effectively mimic through experimentation. This limitation presents a significant obstacle for achieving a comprehensive and unified understanding of cladding degradation mechanisms. Progress is being made to establish a new sensing technique by monitoring cladding and fuels in-core with electrochemical impedance spectroscopy (EIS). Predicted EIS modelling of the corrosion mechanisms can be confirmed with the use of high-resolution characterization techniques, thus providing feasibility of new sensor technology. This work utilizes Raman spectroscopy, scanning Kelvin probe force microscopy (SKPFM), and atom probe tomography (APT) to provide high-resolution characterization of zirconium metal/oxide interfaces. With improved understanding of these techniques, their usability can expand to support EIS sensor technology for in-core operation.

II. EXPERIMENTAL METHODS

Zirconium (Goodfellow) and its alloys Zr-2.65Nb (ATI Metals), Zry-3, and Zry-4 (Idaho National Laboratory) were chosen for the current work (Table I). Samples were isothermally oxidized in a NETZSCH STA-449 F3 Jupiter equipped with thermogravimetric analysis (TGA). Prior to oxidation, samples were prepared by electronic discharge machining (EDM). This was followed by grinding of samples up to 1200 grit SiC and then sonication in 1:1:1 acetone:ethanol:DI solution.

TABLE I. Zirconium alloy compositions.

	Zr (ppm)	Zr-2.65Nb (wt. %)	Zry-3 (wt. %)	Zry-4 (wt. %)
Sn	-	-	0.25	1.4
Fe	200	0.061	0.25	0.2
Cr	200	-	-	0.1
Nb	-	2.62	-	-
C	250	-	-	-
Hf	2500	-	-	-
O	1000	0.106	-	0.12
N	100	-	-	-
H	10	-	-	-

Isothermal oxidation of the samples was done at 700 °C in 80% N_2, 20% O_2 environment. Samples were heated and cooled between room temperature and 700 °C at a 20 °C/min ramp rate. Samples were oxidized in an alumina crucible.

After oxidation, samples were sectioned and mounted in epoxy. They were then ground with SiC up to 1200 grit, followed by polishing with 1 and 0.05 μm alumina slurries. Following polishing, samples were cleaned with Alconox solution on a soft pad, rinsed with ultrapure water, and then air dried. The approximate oxide thickness of each alloy was examined with a Hitachi S-3400N-II (Oxford Instruments Energy+) scanning electron microscope (SEM) at an energy of 10 keV and a 10 mm working distance.

Raman spectroscopy was accomplished using a Horiba LabRAM HR Evolution (Horiba Scientific) with a monochromatic 532 nm laser. Spectral range of 150-700 cm^{-1} was used to examine peaks of interest. Spectra were processed via LabSpec6 with a 'normal variate' normalization, a baseline correction to remove background, and DeNoise smoothing and filtering to enhance spectra. Peak analysis was accomplished with Gaussian-Lorentzian fitting.

SKPFM mapping was done with a Bruker Dimension Icon AFM (Bruker) in an argon filled glovebox. SKPFM is an atomic force microscope (AFM)-variant used to detect the Volta potential difference (VPD) at the nano-scale. PFQNE-AL probes were used to acquire results, operating under a dual-pass method called FM PF-KPFM. The first pass of this method employs PeakForce (PF, Bruker) tapping of the probe at 2 kHz frequency to acquire topographical variations of the surface. Upon completion of a trace and retrace line of topography, the probe lifts off the surface and traces the line of topography at a user-defined lift height of 100 nm, creating a nano-scale scenario synonymous to the traditional Kelvin probe. During this second pass, VPD between probe and surface is measured via probe frequency modulation (FM). This process is repeated line-by-line until a complete map of both topography and relative Volta potential are acquired. Prior to SKPFM mapping of different zirconium alloys, probes were calibrated with a Bruker PFKPFM-SMPL, consisting of n-doped silicon substrate with patterned islands of aluminum surrounded by a gold interconnect. This sample was utilized to ensure relative consistency of probes by providing a step-wise VPD map from gold to silicon to aluminum.[39] Image processing and analysis were conducted using NanoScope Analysis V1.8 (Bruker). Topography maps underwent a flattening process to remove sample tilt.

APT tips were produced with a dual beam FIB/SEM (FEI Quanta 3D FEG) and analyzed with a Local Electrode Atom Probe (LEAP) (CAMECA LEAP 4000X HR). Tips were collected from the metal/oxide interface, providing atomistic make-up of the material surrounding the interface.

III. RESULTS AND DISCUSSION

III.A. Thermogravimetric Analysis

TGA provided observable mass gain rate, and subsequently oxidation rate, for zirconium and its alloys. Pre- and post-breakaway samples were confirmed with

TGA (Figure 1). SEM provided relative thickness of the oxide grown on each sample, as described in Table II.

TABLE II. Approximate oxide thickness of each sample, pre- and post-breakaway, to the nearest 5 μm.

	Oxide Thickness (μm)			
	Zr	Zr-2.65Nb	Zry-3	Zry-4
Pre-break	20	25	10	5
Post-break	100	50	35	30

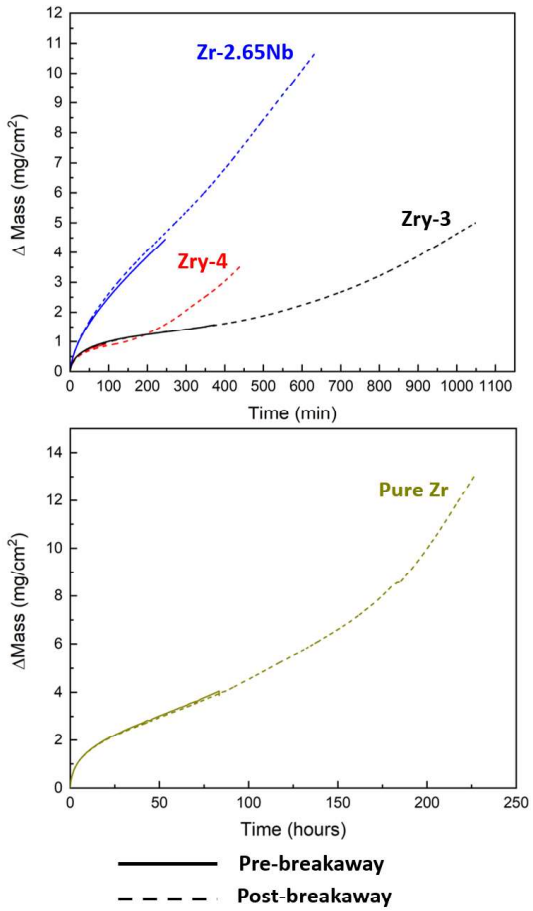

Fig. 1. TGA results for each zirconium alloy exposed to 700°C in 80% N_2, 20% O_2 environment. Pre-breakaway samples are designated with solid lines while dotted lines signify post-breakaway samples.

III.B. Raman Spectroscopy

Raman provides qualitative to semi-quantitative information on the material composition seen in oxides. The Raman spectra of common zirconium-based polymorphs have been extensively covered.[16, 17, 20, 23-26, 28, 29, 40-46] Distinct peaks have been well established for both monoclinic and tetragonal zirconia.[14, 18, 22, 24, 26, 40, 42-44] In particular, Table III describes specific peak positions used in this study. The wide ranges in the tetragonal peak position has been attributed to high compressive stresses observed near the metal/oxide interface, at times even causing distinction between a "relaxed" tetragonal phase and an "interface" tetragonal phase.[16, 20, 27]

TABLE III. Notable tetragonal (T) and monoclinic (M) zirconia Raman peak positions.[16, 20, 25, 27, 29, 44, 46-48]

Attribution	Peak Position (cm^{-1})
M_3	220-224
T_1	262-287
M_4	300-310
M_7	380-384

There has been much discussion about the relationship between the presence of tetragonal zirconia and the stress state. Tetragonal zirconia is thermodynamically stable above 1205 °C,[49] but can be stabilized at lower temperatures by high compressive stress near the metal/oxide interface.[50] Therefore, presently, regions of scale with high tetragonal concentration near the metal/oxide interface should coincide with high compressive stresses. The understanding of this correlation is important, as prior efforts have led to a belief that the formation of tetragonal phase relates to alloy passivity, porosity, and crack formation.

Content of tetragonal phase (i.e., "percent tetragonality") has been estimated as a volume fraction of tetragonal peak intensity versus monoclinic peaks (Equation 1). Different forms of Equation 1 have been used in literature to determine percent tetragonality.[10, 27, 29, 51, 52] The T_1 peak is commonly seen as the most intense tetragonal peak, and thus the T_1 peak versus its adjacent monoclinic peaks (M_3 and M_4) was adopted for calculating percent tetragonality in this work.

$$\%T_{ZrO_2} = \frac{I(T_1)}{I(M_3)+I(T_1)+I(M_4)} x100\% \qquad (1)$$

As for the stress-state, stress development of zirconia has been covered for more than 50 years.[9, 10, 22-27, 53] In particular, Raman spectroscopy has been utilized to observe oxide scales both during heating of a sample,[23-25] as well as with post-exposure examination of sectioned oxides. The stress presented from post-exposure Raman analysis is defined as a residual stress, which comprises of growth, thermal, and relaxation contributions to the stress state.[22] Residual stress is commonly observed by shifts from non-stressed Raman peak positions, where certain peaks are more reliable than others during calibration. Using Raman, residual stress has been calculated between hundreds of MPa to more than 5 GPa at the metal/oxide interface.[22] In one instance, Chong and Fitzpatrick discussed the feasibility of the M_7 peak for residual stress

calculation, warranted by a calibrated peak shift arising from uniaxial compression applied to laboratory-prepared monoclinic zirconia.[10] In general, a direct correlation between shift from expected peak position and residual stress has been shown, where a positive peak shift coordinates to tensile stress and a negative peak shift coordinates to compressive stress.[10] For this work, residual stress is qualitatively observed as a shift from expected M_7 peak position at 381 cm^{-1}.

Percent tetragonality and peak shift (as it relates to residual stress) were observed with Raman of pre- and post-breakaway oxides of zirconium and its alloys. Figure 2 presents these two parameters as a function of distance from the metal/oxide interface of a pre-breakaway Zr sample. The tetragonal-rich region near the metal/oxide interface is clearly seen. The T_1 peak slowly transitions to greater wavenumbers as the distance from the metal/oxide interface increases, until finally it is not visible at the 6 µm spectra and beyond. This corresponds to a rapid decrease in percent tetragonality as the distance from the interface increases. Likewise, a highly compressive stress, relating to a negative shift in the M_7 peak position, is seen near the interface, with the bulk of the oxide expressing a peak shift within a cm^{-1} of the "non-stressed" expected position. Additionally, from this line scan the percent tetragonality and the relative residual stress were compared. The fit of the line scan data displays a general trend where an increase in tetragonality corresponds to an increasingly compressive residual stress, which is in agreement with previous works. However, statistically speaking this linear trend does not fit well to a data, as there is notable scatter (goodness of fit, $R^2 = 0.144$).

This concept of statistically comparing residual stress to percent tetragonality can be expanded from an individual line scan to a full Raman map. Figure 3 presents this idea, observing both the percent tetragonality and M_7 peak position over a 25x40 µm area. Tetragonal-rich zirconia can be seen in the few microns nearest the metal/oxide

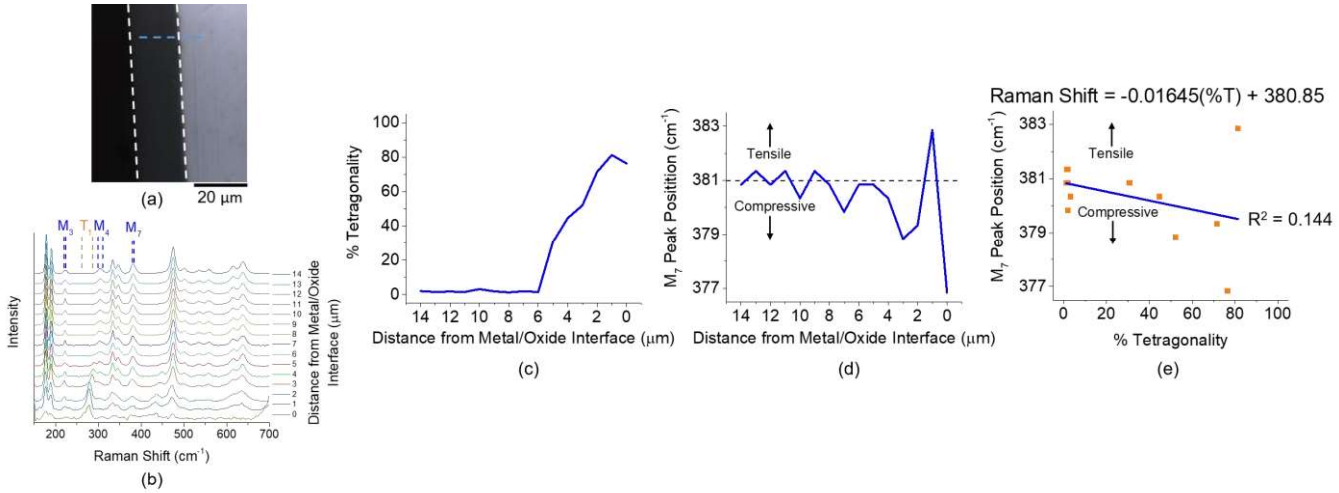

Fig. 2. (a) Optical image of pre-breakaway Zr sectioned sample. White lines separate (left) epoxy/oxide and (right) oxide/metal interfaces. Blue line displays collected Raman line scan. (b) Spectra from collected Raman line scan, with notable peak ranges presented. (c) Percent tetragonality and (d) position of the M_7 peak as a function of distance from the metal/oxide interface. (e) Percent tetragonality as a function of the M_7 peak position.

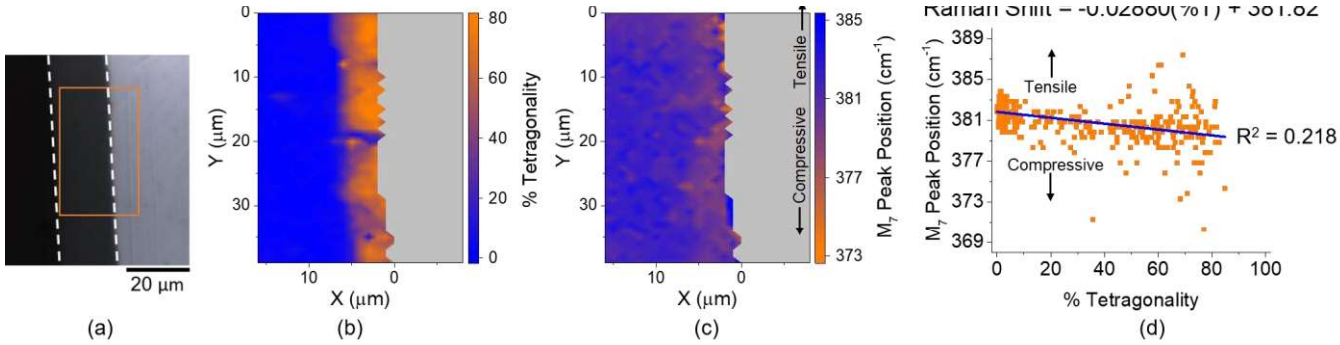

Fig. 3. (a) Optical image of pre-breakaway Zr sectioned sample. White lines separate (left) epoxy/oxide and (right) oxide/metal interfaces. Orange rectangle displays collected Raman map area. (b) Percent tetragonality and (c) position of the M_7 peak as a function of location. Grey represents metal, where Raman peaks are non-apparent. (d) Percent tetragonality as a function of the M_7 peak position for the data collected in the Raman map.

interface, with the bulk of the oxide showing majority monoclinic phase. The trend of M_7 peak position as a function of percent tetragonality for a full map is similar to that of the line scan, where an increase in tetragonality is correlated to a decreasing M_7 peak position, and thus greater compressive stress. Again, though this trend is in agreement with previous works, the data does not appear to fit well to a linear trend. This is especially noticeable when looking at the far right of the plot, where volume fraction of the zirconia is predominantly tetragonal. The distribution for highly tetragonal spectra is large, ranging nearly 20 cm^{-1} in peak position.

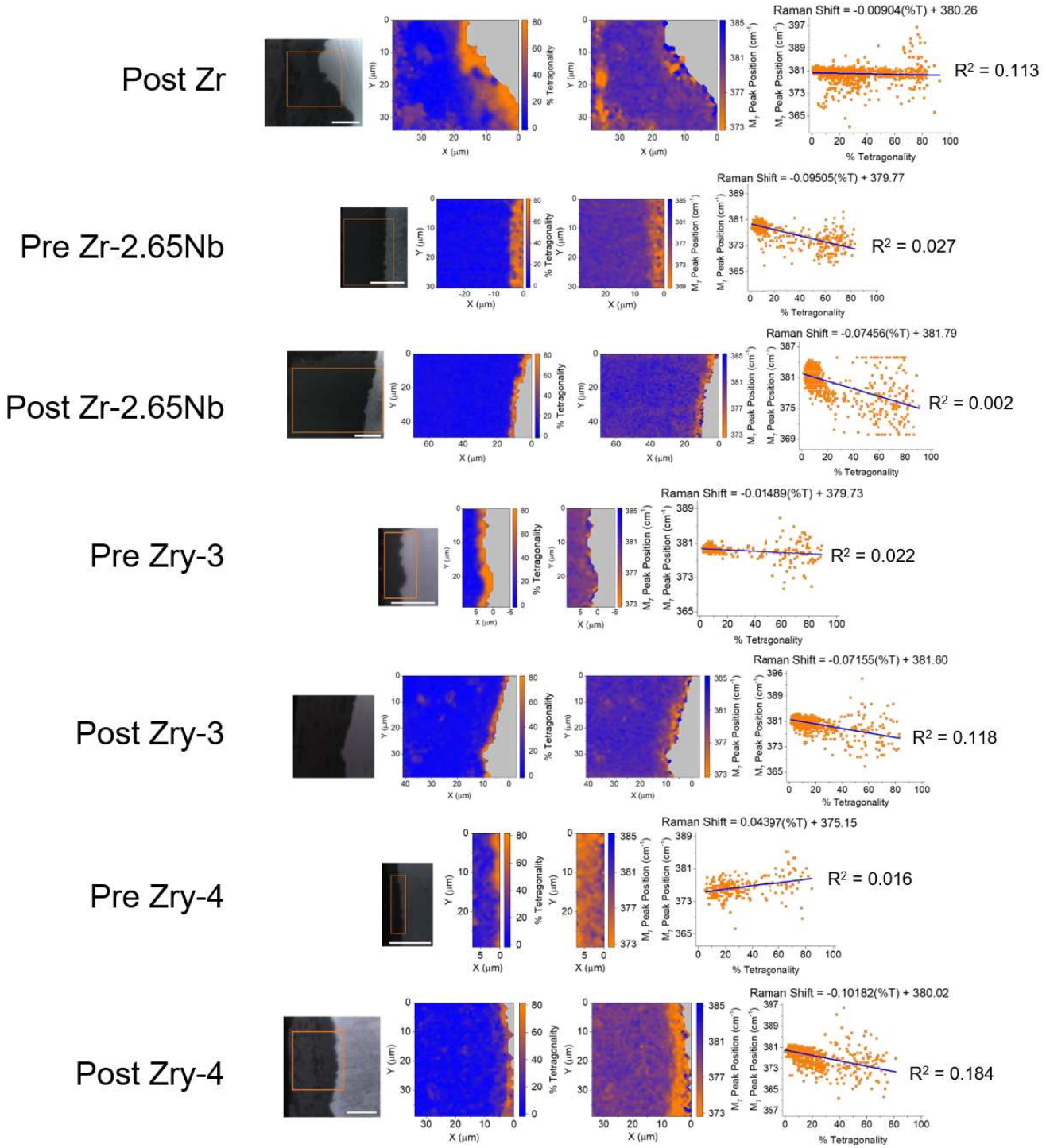

Fig. 4. Raman mapping analysis for post-breakaway Zr, as well as pre- and post-breakaway Zr-2.65Nb, Zry-3, and Zry-4. Metal is shown in grey color.

Similar effects were accomplished for each zirconium alloy, both pre- and post-breakaway (Figure 4). In general, the post-breakaway Zr, Zry-3, and Zry-4 show signs of the "relaxed" tetragonal zone in the bulk of the oxide. Kurpaska et al describe stability of this relaxed tetragonal phase as unrelated to high compressive stress tensor, and rather induced by sub-stoichiometry of the oxide, as it relates to porosity of the scale.[20] In other words, this is a stress-free grown tetragonal zirconia that forms within the bulk of the monoclinic zirconia scale, developed by a lack of available oxygen to form monoclinic zirconia.

All pre-breakaway samples did not display this relaxed tetragonal phase; tetragonal-rich zirconia was seen only in the few microns nearest the metal/oxide interface. The exception to this distinction is the pre-breakaway Zry-4. This Raman map displays high tetragonality on the epoxy side of the oxide, which are observed as "relaxed" tetragonal peaks with lower wavenumbers (e.g., less than 265 cm^{-1}) than those peaks seen in the stress-stabilized tetragonal zirconia at the metal/oxide interface.

As for percent tetragonality and compressive stress, all samples except for Zry-4 pre-breakaway show a general correlation between the two measured parameters. As was stated before, there is a notable increase in scatter for the high percent tetragonality spectra. This could be attributed to the addition of relaxed tetragonal phase in the data. However, this increase in scatter is also seen in Raman maps where no relaxed tetragonal zirconia is seen.

III.C. Scanning Kelvin Probe Force Microscopy

SKPFM mapping provides nano-scale spatial resolution of relative Volta potentials seen at and around the metal/oxide interface for zirconium and its alloy. SKPFM has been used in the corrosion community to quantify relative nobility of different microstructural features for many materials. This technique has yet to be realized with regards to zirconium alloys used in nuclear cladding applications. Figure 5 presents topography and SKPFM maps of pre- and post-breakaway samples.

Segregation between oxide and metal is noted on both topography and potential maps. Interestingly, the measurable Volta potential of the oxide is less than the Volta potential of the metal in each image of pure Zr sample. This is contrary to expectation, as it would be assumed that a ceramic oxide would intrinsically have a greater work function (and thus greater relative Volta potential) than zirconium metal. This contradiction is furthered when observing the Zr-2.65Nb, Zry-3, and Zry-4 SKPFM maps. Here, it can be seen that the oxide consistently displays, as expected, a higher Volta potential than the metal. Also of note is after an initial peak in Volta

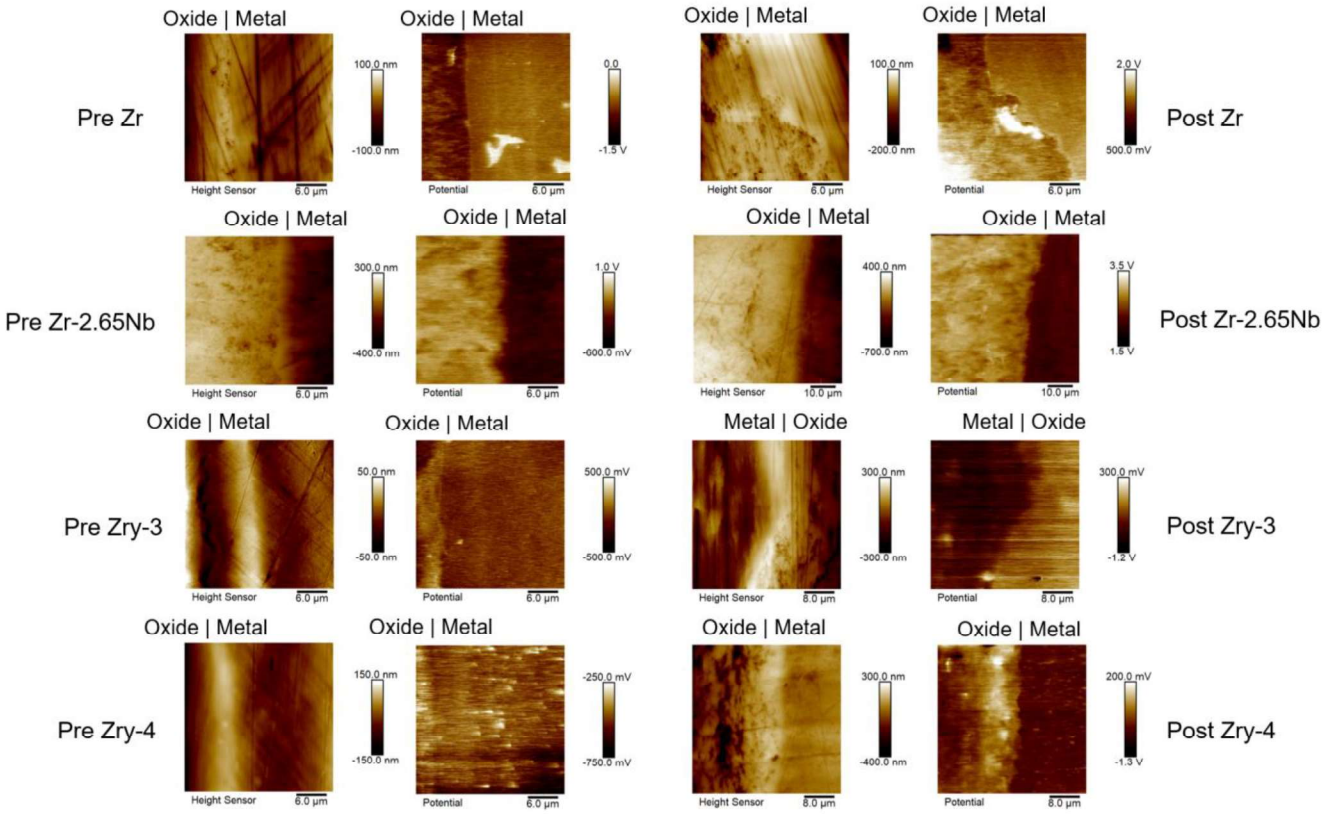

Fig. 5. Topography (left) and Volta potential (right) maps for pre- and post-breakaway Zr, Zr-2.65Nb, Zry-3, and Zry-4. Oxide/metal interfaces are noted in each map.

for the oxide of post-breakaway Zry-4, there is a noticeable drop in the Volta potential. Additionally, micro features are seen in many of the maps, which display much higher potentials than the surroundings (Zr, Zry-3, and Zry-4). This represents a key benefit of SKPFM, which is commonly utilized to recognize phase separation in metal alloys. These secondary particles are likely caused by the inclusions of iron, tin, and/or chromium, which tend to cause phase separation and lattice mismatch in zirconium.

Another benefit of SKPFM is the utility of observing both metal and oxide, rather than solely oxide, as is the case with Raman. With SKPFM, the transition from metal to oxide can be observed.

Plausible future utility of SKPFM is the detection of hydrogen precipitation in the oxide and metal. Hydrogen-enriched zones have been detected with SKPFM on a variety of metals.[54-65] Therefore, SKFPM should be able to provide similar rapid, non-destructive examination of hydrogen embrittlement within zirconium alloys. Establishing SKPFM as a high-resolution characterization technique can potentially improve the understanding of cladding degradation mechanisms.

Co-localized areas of many samples were accomplished with SKPFM and Raman mapping. Co-localization of these two techniques provide the opportunity to compare crystallographic information via Raman to electronic properties via SKPFM. As SKPFM is relatively less destructive, as well as done in an inert environment and is highly sensitive to surface reactions, this technique was done prior to Raman mapping. Co-localization was accomplished on Zr, Zr-2.65Nb, pre-breakaway Zry-3, and post-breakaway Zry-4.

For example, on post-breakaway Zr a similar co-localized feature can be seen near the metal oxide interface, presented as a high VPD particle from SKPFM (Figure 5) and low tetragonality in an otherwise highly tetragonal area from Raman (Figure 4).

III.D. Atom Probe Tomography

APT tips at the metal/oxide interface were successfully acquired and analyzed for pre-breakaway Zr (Figure 6) and post-breakaway Zr-2.65Nb (Figure 7). On the pre-breakaway Zr sample, there is evidence of $Zr(O)_{ads}$ region at the boundary between the metal and oxide, confirming other's results.[7, 35, 66] This is also in agreement with the general oxide formation model presented by Motta et al, where oxygen diffusion forms a metastable region at the interface.[8] On the post-breakaway Zr-2.65Nb sample, a differing composition is seen at the interface. It can be seen that the $Zr(O)_{ads}$ region is much thicker, as both top and bottom of the tip is made up of 52-54 at. % Zr. However, in the middle of these regions there are two different tiers showing closer to 1:1 Zr:O percentages. Additionally, the amount of niobium observed in this volume (ranging from 0.4-0.7 at. %) is much less than expected. It is also notable that there is a high and even distribution of iron across the volume, which is contrary to the concentrated secondary particles observed in Zry-3 and Zry-4 alloys.

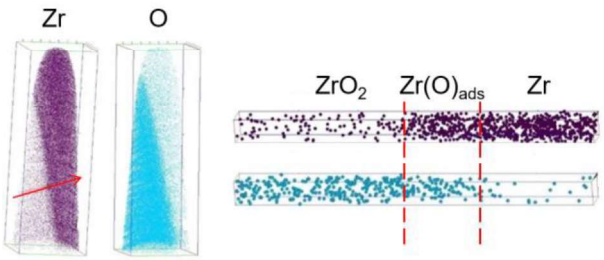

Fig. 6. APT results from pre-breakaway Zr sample. (Left) Tip dimensions are 75.9 x 74.6 x 223.8 nm^3, with the arrow representing a 4 x 4 x 60 nm^3 volume. (Right) 1D concentration profile of zirconium and oxygen, with phases segregated. Fixed bin size of 0.5 nm was used.

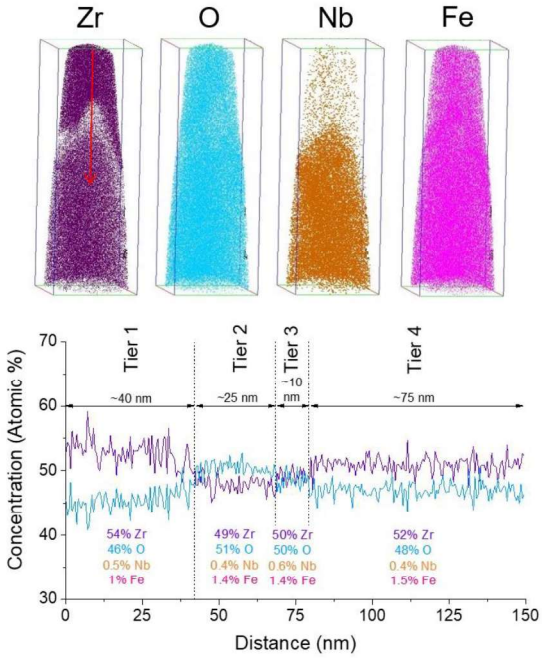

Fig. 7. APT results from post-breakaway Zr-2.65Nb sample. (Top) Tip dimensions are 103.8 x 97.9 x 285.7 nm^3, with the arrow representing a 5 x 5 x 150 nm^3 volume. (Bottom) 1D concentration profile of zirconium and oxygen across the volume, with average concentrations noted in each "tier". Fixed bin size of 0.5 nm was used.

IV. CONCLUSIONS

Observing specific features of Raman spectra can provide insight into the mechanisms at play during zirconium oxide growth. Post-examination Raman of sectioned oxides, with the use of quantitative formulas, provided mapping of percent tetragonality and relative residual stress for Zr, Zr-2.65Nb, Zry-3, and Zry-4 alloys at points before and after breakaway. A general trend of

increasingly compressive stress as a function of increased tetragonal zirconia volume was seen. However, the idea of linear correlation between crystal makeup and stress development is in question; perhaps there are additional factors that support either of these factors, and how they drive the breakaway phenomenon.

SKPFM was used for the first time to examine oxidized zirconium alloys. With SKPFM, distinguishing different phases was accomplish, both at the metal/oxide interface, as well as when observing secondary phase separation. This tool may be feasible to provide further insight into degradation of zirconium alloys, with applications in relative phase nobility, hydrogen detection, and other possible utilities yet to be discovered.

APT was used to observe atomistic make-up of the region about the metal/oxide interface, presenting differences in $Zr(O)_{ads}$ region between pre- and post-breakaway samples. Post-breakaway Zr-2.65Nb showed "tiers" of differing elemental make-up within the $Zr(O)_{ads}$ region.

These different characterization techniques are useful to improve understanding of oxidation mechanisms of zirconium cladding materials. In addition, they can be used to support development of sensors, particularly in confirming EIS modelling of cladding oxide growth.

ACKNOWLEDGMENTS

The authors acknowledge the In-Pile Instrumentation Initiative (I2) sponsored by the Department of Energy (DOE). Paul H. Davis, Elton Graugnard, and Bill Knowlton of the Boise State Surface Science Laboratory, as well as Jatuporn Burns and Megha Dubey of CAES are thanked for their support. FIB and APT were done at Microscopy and Characterization Suite (MaCS) in CAES. The authors also acknowledge the departmental support from Boise State's Micron School of Materials Science and Engineering.

REFERENCES

1. N. STOJILOVIC, *et al.*,"Surface chemistry of zirconium" *Prog Surf Sci,* **78** (3-4), (2005).
2. A. COUET, *et al.*,"In-situ electrochemical impedance spectroscopy measurements of zirconium alloy oxide conductivity: Relationship to hydrogen pickup" *Corros Sci,* **119** (2017).
3. B. COX,"Some thoughts on the mechanisms of in-reactor corrosion of zirconium alloys" *Journal of Nuclear Materials,* **336** (2-3), (2005).
4. B. COX,"The Oxidation and Corrosion of Zirconium and Its Alloys .5. Mechanism of Oxide Film Growth and Breakdown on Zirconium and Zircaloy-2" *J Electrochem Soc,* **108** (1), (1961).
5. C. PROFF, *et al.*,"Oxidation behaviour of binary zirconium alloys containing intermetallic precipitates" *Journal of Nuclear Materials,* **416** (1-2), (2011).
6. J. WEI, *et al.*,"The effect of Sn on autoclave corrosion performance and corrosion mechanisms in Zr-Sn-Nb alloys" *Acta Mater,* **61** (11), (2013).
7. N. NI, *et al.*,"How the crystallography and nanoscale chemistry of the metal/oxide interface develops during the aqueous oxidation of zirconium cladding alloys" *Acta Mater,* **60** (20), (2012).
8. A. T. MOTTA, *et al.*,"Corrosion of Zirconium Alloys Used for Nuclear Fuel Cladding" *Annu Rev Mater Res,* **45** (2015).
9. D. H. BRADHURST and P. M. HEUER,"Influence of Oxide Stress on Breakaway Oxidation of Zircaloy-2" *Journal of Nuclear Materials,* **37** (1), (1970).
10. K. B. CHONG and M. E. FITZPATRICK,"Evolution of stress fields and phase content in corroded zirconium cladding materials" *Surf Coat Tech,* **324** (2017).
11. A. COUET, *et al.*,"The coupled current charge compensation model for zirconium alloy fuel cladding oxidation: I. Parabolic oxidation of zirconium alloys" *Corros Sci,* **100** (2015).
12. M. OSKARSSON, *et al.*,"Oxidation of Zircaloy-2 and Zircaloy-4 in water and lithiated water at 360 degrees C" *Journal of Nuclear Materials,* **295** (1), (2001).
13. A. ZIELINSKI and S. SOBIESZCZYK,"Hydrogen-enhanced degradation and oxide effects in zirconium alloys for nuclear applications" *Int J Hydrogen Energ,* **36** (14), (2011).
14. C. DURIEZ, *et al.*,"Reaction in air and in nitrogen of pre-oxidised Zircaloy-4 and M5 (TM) claddings" *Journal of Nuclear Materials,* **441** (1-3), (2013).
15. C. DURIEZ, *et al.*,"Zircaloy-4 and M5 (R) high temperature oxidation and nitriding in air" *Journal of Nuclear Materials,* **380** (1-3), (2008).
16. I. IDARRAGA, *et al.*,"Potentialities of Raman Imaging for the Analysis of Oxide Scales Formed on Zircaloy-4 and M5 (R) in Air at High Temperature" *Oxid Met,* **79** (3-4), (2013).
17. I. IDARRAGA, *et al.*,"Raman investigation of pre- and post-breakaway oxide scales formed on Zircaloy-4 and M5 (R) in air at high temperature" *Journal of Nuclear Materials,* **421** (1-3), (2012).
18. M. LASSERRE, *et al.*,"Modelling of Zircaloy-4 accelerated degradation kinetics in nitrogen-oxygen mixtures at 850 degrees C" *Journal of Nuclear Materials,* **462** (2015).
19. M. LASSERRE, *et al.*,"Qualitative analysis of Zircaloy-4 cladding air degradation in O-2-N-2 mixtures at high temperature" *Mater Corros,* **65** (3), (2014).
20. L. KURPASKA, *et al.*,"Raman spectroscopy analysis of air grown oxide scale developed on pure zirconium substrate" *Journal of Nuclear Materials,* **466** (2015).

21. E. T. HAYES and A. H. ROBERSON,"Some Effects of Heating Zirconium in Air, Oxygen, and Nitrogen" *J Electrochem Soc,* **96** (3), (1949).
22. M. GUERAIN, *et al.*,"Review of stress fields in Zirconium alloys corrosion scales" *Corros Sci,* **95** (2015).
23. L. KURPASKA, *et al.*,"On the determination of growth stress during oxidation of pure zirconium at elevated temperature" *Appl Surf Sci,* **446** (2018).
24. L. KURPASKA, *et al.*,"In-situ stress analysis of the Zr/ZrO2 system as studied by Raman spectroscopy and deflection test in monofacial oxidation techniques" *Appl Surf Sci,* **385** (2016).
25. L. KURPASKA, *et al.*,"Shift in low-frequency vibrational spectra measured in-situ at 600 degrees C by Raman spectroscopy of zirconia developed on pure zirconium and Zr-1%Nb alloy" *J Mol Struct,* **1126** (2016).
26. L. KURPASKA, *et al.*,"Stress analysis of zirconia studied by Raman spectroscopy at low temperatures" *Spectrochim Acta A,* **131** (2014).
27. L. KURPASKA, *et al.*,"Zirconia Layer Formed by High Temperature Oxidation of Pure Zirconium: Stress Generated at the Zirconium/Zirconia Interface" *Oxid Met,* **79** (3-4), (2013).
28. P. BARBERIS, *et al.*,"Raman spectra of tetragonal zirconia: powder to zircaloy oxide frequency shift" *Journal of Nuclear Materials,* **288** (2-3), (2001).
29. P. BARBERIS, *et al.*,"On Raman spectroscopy of zirconium oxide films" *Journal of Nuclear Materials,* **246** (2-3), (1997).
30. O. I. MALYI, *et al.*,"Formation and migration of oxygen and zirconium vacancies in cubic zirconia and zirconium oxysulfide" *Solid State Ionics,* **212** (2012).
31. C. DURIEZ, *et al.*,"Separate-effect tests on zirconium cladding degradation in air ingress situations" *Nucl Eng Des,* **239** (2), (2009).
32. M. STEINBRUCK and M. BOTTCHER,"Air oxidation of Zircaloy-4, M5 (R) and ZIRLO (TM) cladding alloys at high temperatures" *Journal of Nuclear Materials,* **414** (2), (2011).
33. M. STEINBRUCK, *et al.*,"Oxidation of Advanced Zirconium Cladding Alloys in Steam at Temperatures in the Range of 600-1200 degrees C" *Oxid Met,* **76** (3-4), (2011).
34. M. STEINBRUCK,"Prototypical experiments relating to air oxidation of Zircaloy-4 at high temperatures" *Journal of Nuclear Materials,* **392** (3), (2009).
35. B. DE GABORY, *et al.*,"EELS and atom probe tomography study of the evolution of the metal/oxide interface during zirconium alloy oxidation" *Journal of Nuclear Materials,* **462** (2015).
36. D. R. OLANDER, *et al.*,"Chemical processes in defective LWR fuel rods" *Journal of Nuclear Materials,* **248** (1997).
37. B. MICHEL, *et al.*,"3D fuel cracking modelling in pellet cladding mechanical interaction" *Eng Fract Mech,* **75** (11), (2008).
38. H. K. JENSSEN, *et al.*,"PIE results and mechanistic interpretation on on-line EIS data from the cladding corrosion test IFA-731" (2017).
39. C. M. EFAW, *et al.*,"Toward Improving Ambient Volta Potential Measurements with SKPFM for Corrosion Studies" *J Electrochem Soc,* **166** (11), (2019).
40. C. CISZAK, *et al.*,"Micro-Raman analysis of the fuel-cladding interface in a high burnup PWR fuel rod" *Journal of Nuclear Materials,* **495** (2017).
41. A. KASPERSKI, *et al.*,"High-Temperature Oxidation of Zircaloy-4 in Air Studied with Labeled Oxygen and Raman Imaging" *Oxid Met,* **87** (3-4), (2017).
42. L. KURPASKA, *et al.*,"Identification of the Zirconia Phases by Means of Raman Spectroscopy for Specimens Prepared by FIB Lift-Out Technique" *Oxid Met,* **88** (3-4), (2017).
43. M. GUERAIN, *et al.*,"The use of micro-Raman imaging to measure O-18 tracer distribution in thermally grown zirconia scales" *Corros Sci,* **98** (2015).
44. H. Y. MI, *et al.*,"Monitoring the oxidation of nuclear fuel cladding using Raman spectroscopy" *Journal of Nuclear Materials,* **445** (1-3), (2014).
45. M. ISHIGAME and T. SAKURAI,"Temperature-Dependence of Raman-Spectra of Zro2" *J Am Ceram Soc,* **60** (7-8), (1977).
46. C. M. PHILLIPPI and K. S. MAZDIYASNI,"Infrared and Raman Spectra of Zirconia Polymorphs" *J Am Ceram Soc,* **54** (5), (1971).
47. V. G. KERAMIDAS and W. B. WHITE,"Raman-Scattering Study of Crystallization and Phase-Transformations of Zro2" *J Am Ceram Soc,* **57** (1), (1974).
48. G. G. SIU, *et al.*,"Variation of fundamental and higher-order Raman spectra of ZrO2 nanograins with annealing temperature" *Phys Rev B,* **59** (4), (1999).
49. O-Zr Phase Diagram" *ASM Int., Diagram No. 101191,* (2009).
50. S. BLOCK, *et al.*,"Pressure-Temperature Phase-Diagram of Zirconia" *J Am Ceram Soc,* **68** (9), (1985).
51. D. R. CLARKE and F. ADAR,"Measurement of the Crystallographically Transformed Zone Produced by Fracture in Ceramics Containing Tetragonal Zirconia" *J Am Ceram Soc,* **65** (6), (1982).
52. J. GODLEWSKI, *et al.*,"*ASTM-STP,* **1132** (1991).
53. L. KURPASKA,"Structural properties of zirconia - in-situ high temperature XRD characterization" *J Mol Struct,* **1163** (2018).
54. Z. L. HUA, *et al.*,"Scanning Kelvin probe force microscopy study on hydrogen distribution in austenitic stainless steel after martensitic transformation" *Mater Lett,* **245** (2019).

55. Z. L. HUA, *et al.*,"The finding of hydrogen trapping at phase boundary in austenitic stainless steel by scanning Kelvin probe force microscopy" *Scripta Mater,* **162** (2019).
56. Z. L. HUA, *et al.*,"Hydrogen distribution at twin boundary in austenitic stainless steel studied by scanning Kelvin probe force microscopy" *Mater Lett,* **234** (2019).
57. Z. L. HUA, *et al.*,"The finding of crystallographic orientation dependence of hydrogen diffusion in austenitic stainless steel by scanning Kelvin probe force microscopy" *Scripta Mater,* **131** (2017).
58. S. KOLSCH, *et al.*,"Kelvin probe force microscopy studies of the charge effects upon adsorption of carbon nanotubes and C-60 fullerenes on hydrogen-terminated diamond" *J Appl Phys,* **123** (1), (2018).
59. M. C. LAFOURESSE, *et al.*,"A Kelvin probe force microscopy study of hydrogen insertion and desorption into 2024 aluminum alloy" *J Alloy Compd,* **722** (2017).
60. S. EVERS, *et al.*,"Hydrogen detection in metals: a review and introduction of a Kelvin probe approach" *Sci Technol Adv Mat,* **14** (1), (2013).
61. C. LARIGNON, *et al.*,"Investigation of Kelvin probe force microscopy efficiency for the detection of hydrogen ingress by cathodic charging in an aluminium alloy" *Scripta Mater,* **68** (7), (2013).
62. L. OGER, *et al.*,"Hydrogen diffusion and trapping in a low copper 7xxx aluminium alloy investigated by Scanning Kelvin Probe Force Microscopy" *Mat Sci Eng a-Struct,* **706** (2017).
63. G. WANG, *et al.*,"Investigation of hydrogen evolution and enrichment by scanning Kelvin probe force microscopy" *Electrochem Commun,* **35** (2013).
64. W. BURGSTALLER, *et al.*,"Challenges in hydrogen quantification using Kelvin probe technique at different levels of relative humidity" *J Solid State Electr,* **21** (6), (2017).
65. C. SENOZ, *et al.*,"Scanning Kelvin Probe as a highly sensitive tool for detecting hydrogen permeation with high local resolution" *Electrochem Commun,* **13** (12), (2011).
66. Y. DONG, *et al.*,"Atom probe tomography study of alloying element distributions in Zr alloys and their oxides" *Journal of Nuclear Materials,* **442** (1-3), (2013).